Article

The Effect of Structure and Mechanical Properties Change of Current Collector during Cycling on Sb-Based Lithium-Ion Batteries' Performance

Songnan Zhao [1,2], Weijia Meng [1,2], Genwei Wang [1,2,3], Chunli Guo [4], Shengguo Ma [1,2,3], Zhipeng Lei [5], Yuanyuan Li [5], Meiqing Guo [1,2,3,*] and Hui Song [1,2,3,*]

1   Institute of Applied Mechanics, College of Mechanical and Vehicle Engineering, Taiyuan University of Technology, Taiyuan 030024, China
2   Shanxi Key Laboratory of Material Strength & Structural Impact, College of Mechanical and Vehicle Engineering, Taiyuan University of Technology, Taiyuan 030024, China
3   National Demonstration Center for Experimental Mechanics Education, Taiyuan University of Technology, Taiyuan 030024, China
4   College of Materials Science and Engineering, Taiyuan University of Technology, Taiyuan 030024, China
5   College of Electrical and Power Engineering, Taiyuan University of Technology, Taiyuan 030024, China
*   Correspondence: guomeiqing@tyut.edu.cn (M.G.); songhui@tyut.edu.cn (H.S.)

Abstract: Here, we investigate structure and mechanical change of Cu and Al current collector during cycling and analyze the contribution to capacity attenuation of Sb-based lithium-ion batteries (LIBs). There exists migration of C, Sb, and Li atoms to the inside of Cu current collector, and diffusion of Li, Co, and O atoms to the inside of Al current collector during cycling, which results in the formation of a porous film of Li_2SbCu (with the thickness of 21 μm after 100 cycles) and a relatively dense film of Al_2O_3 (with the thickness of 23 μm after 100 cycles) on the surface of Cu and Al current collector, respectively. The formation of films results in a weak bond between active layer and current collector, and the increase of hardness of 0.84 GPa and modulus of 22.5 GPa for Cu current collector after 100 cycles, which is adverse to the charge capacity and cycling stability. Nevertheless, Al_2O_3 films caused hardness decrease of 0.53 GPa and modulus decrease of 18.93 GPa of Al current collector after 100 cycles, which contributes to the improvement of cycling stability and charge capacity. This study provides an understanding of the capacity loss of Sb-based LIBs from the perspective of structural degradation of current collectors.

Keywords: Sb-based lithium-ion batteries; current collector; mechanical properties; Al_2O_3 film; Li_2SbCu film

1. Introduction

The depletion and environmental issues of fossil energy call for the development of renewable resources, such as sunlight and wind. Thus, it is of importance to look for the energy storage devices to store energy harvested from renewable resources [1–4]. Lithium-ion batteries (LIBs) are promising clean energy devices due to their unique electrochemical energy storage mode, high energy density, adequate working voltage, and long cycle life [5–7]. To date, LIBs have been widely applied in portable electronics devices and electric/hybrid electric vehicles. Nevertheless, with the increase of energy demand, the application of LIBs based on graphite cathode materials has been limited owing to the low theoretical specific capacity of graphite (372 mAh g^{-1}) [8]. Therefore, it is of importance to develop LIBs with high energy and capacity density [9–11]. Carbon-, silicon-, germanium-, antimony-, and titanium-based anode materials have been widely reported because of the high theoretical capacity densities [12,13]. Especially, Sb has been extensively investigated as a substitutable material to graphite in LIBs because of its high theoretical specific capacity and mild reaction platform [14–16]. However, the nonreversible capacity decay

after the electrochemical cycle and the short cycle life of Sb-based anode materials limit their application in LIBs [17–19].

It is generally considered that the aforementioned capacity attenuation and poor cycle stability of Sb-based anode materials are due to the volume strain of up to 150% during the electrochemical cycle [20]. In details, during Sb alloying/dealloying process, the irreversible formation of Li_xSb alloy caused expansion/strain stress, which leads to the crushing of the Sb particles in the anode, and the formation and extension of fissures on the electrode [21]. Furthermore, this behavior will result in the fragmentation of an originally formed solid electrolyte interface (SEI) layer and the formation of a new SEI membrane, which results in the continuous loss of lithium ions and the separation between the active materials layer and the current collector after multi cycles [22,23]. The continuous occurrence of the foregoing changes finally results in the mechanical stability decrease of electrode and the reversible capacity attenuation of anode materials [24].

In addition, it is reported that the electrochemical performance of LIBs is related to morphology, mechanical properties, and anti-corrosion characteristics [25–32]. Zhang [25] reported the dissolution of Cu collector in electrolyte under 3.5–4.5 V and the dissolution of Al collector over 3.0 V. Lee [26] studied the cycling performance of the electrode slurry on the copper collector with different surface morphology and found that nodule-type foil is quite effective for improving the cycle performance for Si-based electrodes. Guo [27] developed an electrochemical mechanical representative volume element model to study the contact behavior of porous electrodes. The decrease in the elastic modulus of the collector increases the contact radius and reduces the contact stress. Compared with the smooth current collectors, rough current collectors have a smaller contact area and larger contact stress when contacting active particles. Tang [28] reduced the roughness of electrolytic copper foil with electropolishing. The results show that copper foil with low roughness has high electrical conductivity, which can effectively improve the uniformity of graphite anode coating. The contact area between low roughness copper foil and electrolyte is small, and the corrosion resistance is stronger. HJ Ahn et al. [29,30] fabricated the porous structure on the surface of pure metal Al current collector and the carbon quantum dots-coated stepped porous Al current collector, which was unitized as the cathode current collector. It is found that the electrochemical cycling and ultrafast discharge performance of LIBs can be enhanced due to the excellent conductivity and enlarged contact area between the active materials layer and the current collector. L Roué et al. [31] found that rough surface morphology of Cu current collector can enhance the adhesion of active materials to the Cu current collector, which contributes to the improvement of reversible capacity and cycling stability. Similar results were also obtained by WB Jung and HT Jung [32], and they fabricated the LIBs with a wrinkled Cu as the current collector and believed that the improved electrochemical cycling should be attributed to the enhanced adhesion between active materials and the current collector.

All investigations have confirmed the importance of morphology roughness, mechanical properties, conductivity, and anti-corrosion characteristics of the current collector before cycling to the performance of LIBs. Meanwhile, in our previous work, we found that there exists the migration of Li, C, and O atoms towards the Cu current collector during electrochemical cycling [33], resulting in some changes of composition, structure, and conductivity of current collector. Also, Hyams et al. [34] reported that the dissolved Al element exists in the electrolyte, and the amount of Al in the electrolyte increases with the number of cycles and the temperature, which confirmed the corrosion of Al during cycling. However, a few investigations are focused on this performance change of Cu and Al current collectors after cycling and the corresponding effect on the performance degradation of LIBs. Therefore, it is important to clarify the microstructure and performance change of Cu and Al current collectors during repeated discharge/charge process, and the effect mechanism on capacity decrease of Sb-based LIBs.

Accordingly, in this study, we investigate the change of the Cu and Al current collector in Sb-based lithium-ion full batteries and analyze its contribution to the capacity decrease.

We have assembled LIBs using Sb nanocrystal-anchored hollow carbon microspheres (Sb@HCMs)/Cu anode and LiCoO$_2$/Al cathode (the detailed information of Sb@HCMs, LiCoO$_2$ and the electrochemical performance of LIBs with Sb@HCMs/Cu anode and LiCoO$_2$/Al have been reported in our previous work [35]), and investigate the morphology, composition, phase structure, and local deformation behavior of Cu current collector and Al current collector after different cycles. Also, the change of current collector and its detailed effect on the performance of LIBs were analyzed. This study provides novel thinking for the capacity decrease of Sb-based LIBs, and guidance for the design and surface modification of current collector.

2. Materials and Methods

2.1. Synthesis of Nano Sb@HCMs

The synthesis and structure details of Sb@HCMs and LiCoO$_2$, and the assemble and electrochemical performance of Sb@HCMs/Cu//LiCoO$_2$/Al full cells have been reported in our previous work [35]. In brief, 0.1 g of yeast was dispersed in 5 mL of culture medium and kept for 24 h at 37 °C. The suspension was centrifuged at 6000 r min^{-1} for 10 min and washed by NaCl solution (0.15 mM) three times. The as-collected yeast cells were fixed by 10 mL of glutaraldehyde (2.5%) at 4 °C oven overnight, dehydrated using sequential ethanol of 20%, 20%, 80%, 90%, and 100%, and calcined in air for 2 h at 300 °C to form hollow carbon microspheres (HCMs). Then, HCMs (0.1 g) and SbCl$_3$ (0.8 g) were magnetically dispersed in ethylene glycol, and subsequently the NaBH$_4$ solution (0.1 M, 12 of pH) was added. Finally, the mixture was kept at 60 °C for 2 h and collected after being washed with deionized water and ethanol five times. The Sb nanocrystal-anchored hollow carbon microspheres (Sb@HCMs) were obtained by being centrifugated at 8000 r min^{-1} for 10 min and dried at 60 °C for 5 h in a vacuum. All raw chemicals are of analytical grade and used as received without other treatment.

2.2. Materials Characterization

A field emission scanning electron microscope (SEM, JSM-7100F, JEOL, Tokyo, Japan) was used to observe the surface and section morphology. Precision Ion Polishing System (Gatan 691, Gatan, Pleasanton, CA, USA) and high resolution transmission electron microscopy (HRTEM, Tecnai-G2F20, FEI, Hillsboro, USA) was used to observe the lattice fringes. X-ray powder diffractometer (XRD, RigakuD/MAX-2500, Cu-Ka, λ = 1.54178 A, Rigaku, Tokyo, Japan) and Energy dispersion X-ray spectrometer (EDX, XM 20, OXFORD, Oxford, UK) were used to analyze the crystal structure and composition. The indenter used in the experiment is Bosch triangular pyramid indenter, which is easy to operate and can produce plastic deformation under a small load. The nanoindentation experiment method of continuous stiffness was adopted. The indentation speed is 10 nm s^{-1}, the frequency is 45 Hz, and the loading strain rate is 0.05 s^{-1}. Figure 1 depicts a schematic diagram of the parameters of the press head when pressed into the material and after unloading, where h is the full depth, h$_c$ is the contact depth, and h$_s$ is the displacement of the surrounding material at the compression.
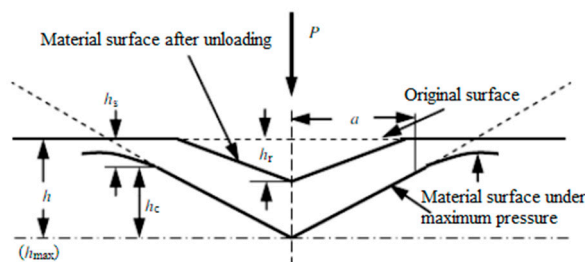

Figure 1. Schematic diagram of indenter pressing material and parameters after unloading.

2.3. Electrochemical Characterization

The 2032-type coin full LIBs were assembled in an Ar glove box. The cathode was fabricated by pasting the slurry consisting of Sb@HCMs, acetylene black and carboxymethyl cellulose with a mass ratio of 6:3:1 on the bare Cu disk with a diameter of 12 mm. Similarly, the active materials layer in the anode was composed of 80% of $LiCoO_2$, 10% of acetylene black and 10% of polyvinylidene fluoride, and the current collector was Al foil with a diameter of 14 mm. The separator and electrolyte were a Celgard 2400 (Celgard, LLC, Charlotte, NC, USA) and 1 M $LiPF_6$ in carbonate(EC)/dimethyl carbonate(DMC)/diethyl carbonate(DEC) with a volume ratio of 1:1:1. The full LIBs cycled to the 1st, 10th, 30th, 50th, and 100th cycle at the current density of 0.1 A g^{-1} from 0.01 V to 2 V versus Li/Li^+, and disassembled in an Ar atmosphere glove box. The Cu and Al current collectors for the experiment were washed by EC/DMC/DEC. All raw materials are analytical and used without other treatment.

3. Results and Discussion

3.1. Morphology, Structure, and Mechanical Performance Evolution of Cu Current Collector during Cycling

3.1.1. Morphology and Structure Analysis

The phase structure of Cu is analyzed by XRD, and the results are shown in Figure 2a. From Figure 2a, the diffraction peak at 43.34°, 50.47°, and 70.18° can be assigned to the (1 1 1), (2 0 0), and (2 2 0) crystal face of cubic Cu. The (0 0 2) crystal plane of carbon can also be observed according to the wide diffraction peak in the range of 20°~30°, which increases with the increase of cycle number. More C atoms in the active materials layer are suggested to diffuse into the tetrahedron and the octahedron voids of cubic Cu. The weak and small diffraction peaks at 24.58°and 74.032° indicate the formation of Li_2SbCu alloy phase, which is associated with the migration of Sb and Li atoms to the Cu current collector.
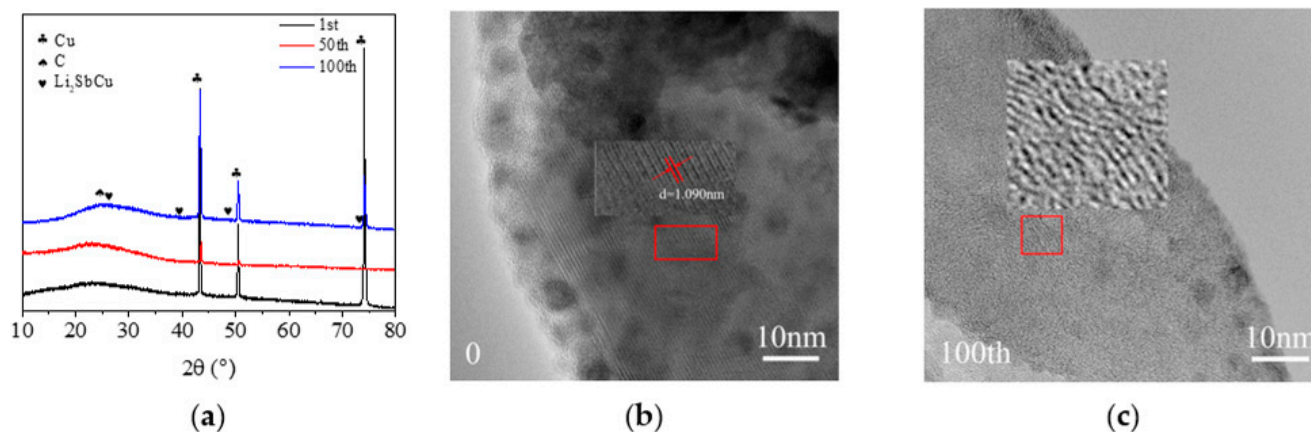

Figure 2. (**a**) XRD patterns of the Cu current collector disassembled from LIBs after different discharge/charge cycles. HRTEM images of the Cu foils disassembled from the LIBs before (**b**) and after (**c**) 100 cycles. The insert of (**b**,**c**) is enlarged portion of corresponding red area.

To further confirm the migration of Li, C, Cu, Sb between the active materials layer and the Cu foil and their distribution change along with the cross-section during discharge/charge process, the HRTEM scans of the Cu foil before and after different cycles are performed. The HRTEM images of Cu foils before and after 100 cycles are shown in Figure 2b,c. From Figure 2b, for Cu foils disassembled from the LIBs without cycling, the lattice spacing is 1.090 nm, which corresponds to the (3 1 1) crystal plane of cubic Cu. From Figure 2c, the lattice fringes of after 100 cycles are disordered, which can be attributed to the existence of C atoms in the porous layer and weak crystallinity of Li_2SbCu in the porous layer. It is speculated that the migration of C, Sb, and Li atoms into the copper foil during the electrochemical cycle destroys the original crystallinity of the copper foil.

The surface microphotographs of Cu foils in LIBs, which cycled to the 0, 1st, 10th, 30th, 50th, and 100th cycle, are shown in Figure 3. From Figure 3, the Cu foil has a relatively dense surface with irregular bulges, and the width of gaps among bulges is 250–350 nm before the discharge/charge process (Figure 3a). When the LIBs experienced one discharge/charge cycle, the surface of the Cu foil becomes rougher than that before cycling, and the width of cracks among irregular bulges is ~700 nm (Figure 3b). As speculated, for Cu foils obtained from the LIBs after ten and thirty cycles, the crack size among bulges increases with increasing the discharge/charge cycle (Figure 3c,d). The rough surface and the increased crack size may be due to the corrosion of Cu foil in HF produced by the disintegration of $LiPF_6$ during discharge/charge cycles. Kawakita and Kobayashi [36] revealed that the formation of irregular bulges and the width of gaps on the surface of Cu is related to the oxidation and corrosion of Cu in the electrolyte. Interestingly, part of the cracks among bulges vanished after fifty and one hundred cycles, which is attributed to the fill of electrochemical reaction sediment between electrode material and electrolyte.
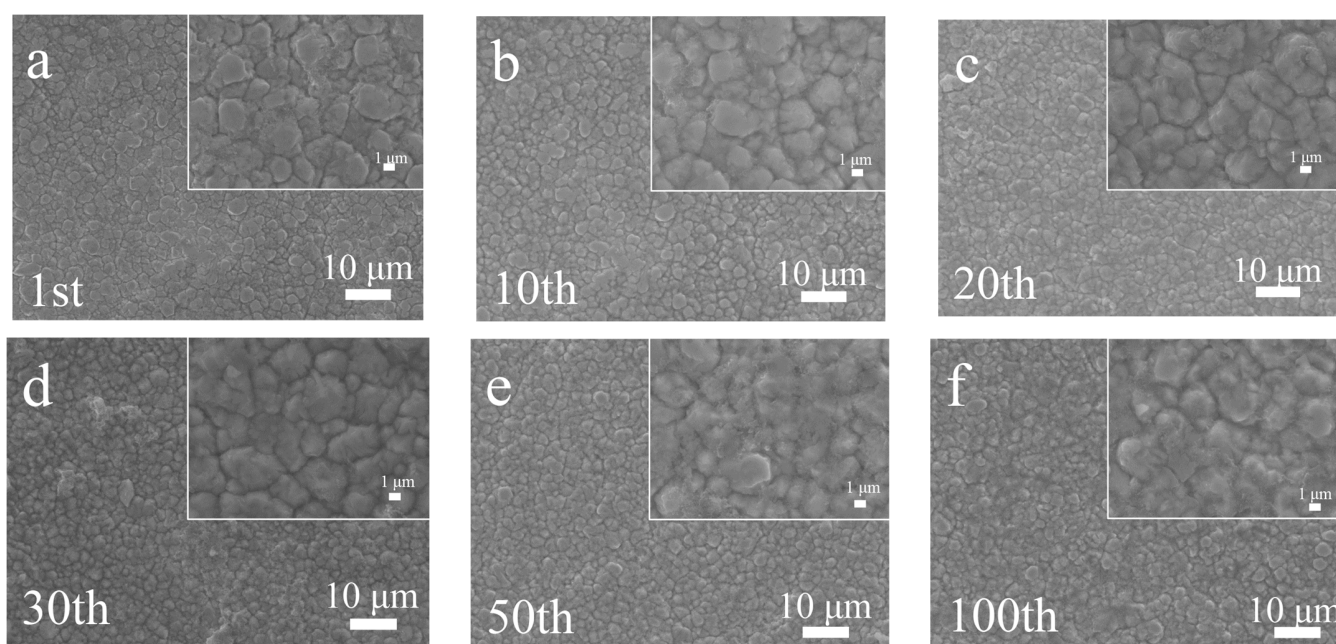
Figure 3. SEM microphotographs of the surface of Cu foils disassembled from the LIBs before (**a**) and after (**b**–**f**) different cycles.

From Figure 4, the original Cu foil has a smooth, continuous, and dense cross-section with no gaps (Figure 4a). For the Cu foil disassembled from the LIBs after one cycle, a thin and porous film is observed on the surface of the Cu foil, and no obvious separation between this porous film and Cu foil can be found (Figure 4b). It is speculated that the loose and porous film is caused by continuous corrosion of Cu by HF and migration of atoms in active materials layer to Cu foil. With the prolonging of discharge/charge cycling to ten and fifty cycles, there is an obvious thickness increase of the porous film and visible local separation between porous film and Cu foil (Figure 4c,d). When the LIBs experienced one hundred cycles, large gaps were formed between porous film and Cu foil (Figure 4e). It is certain that the current collector consists of the original Cu foil and the new-formed porous film after the discharge/charge process and the thickness of the current foils increases. This microstructure change will impair the conductivity and mechanical stability of current collector finally causinghe capacity and stability decrease of LIBs. The thickness change of the original Cu foil and the new-formed porous film during the discharge/charge process is shown in Figure 4f.
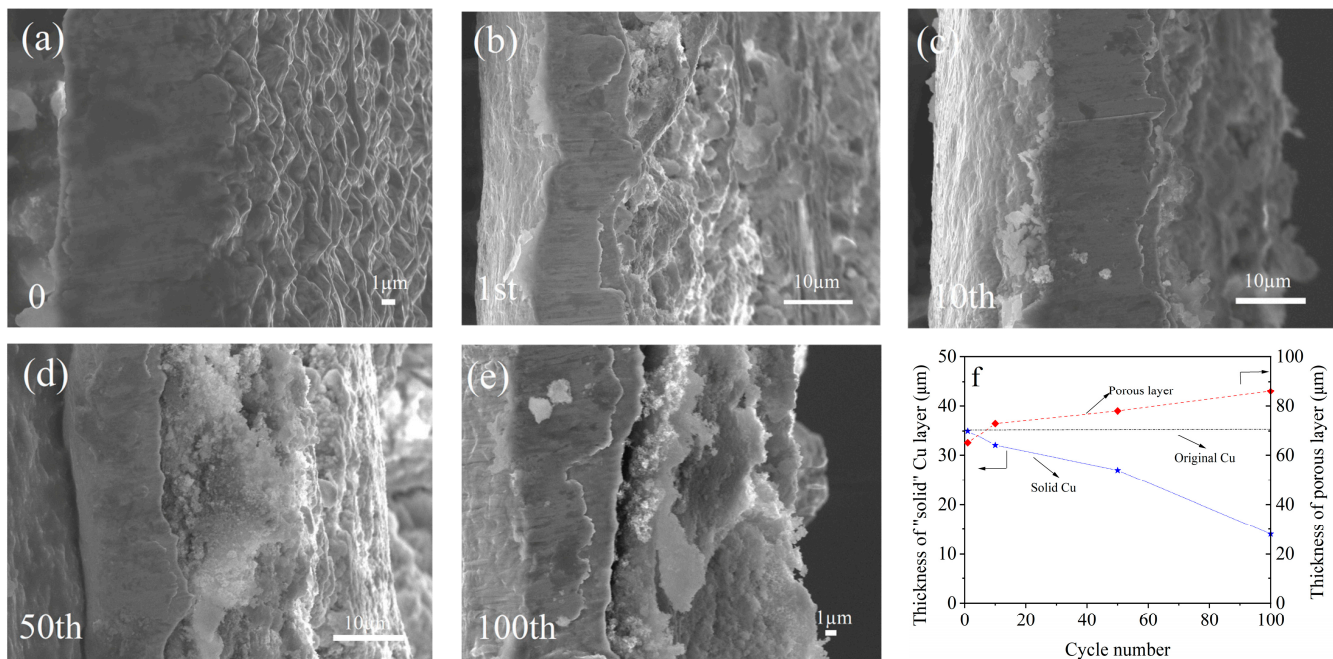
Figure 4. SEM microphotographs (**a**–**e**) of the cross-section of Cu foils disassembled from the LIBs after different cycles, and (**f**) thickness change of the Cu foil during the discharge/charge process.

From Figure 5a, only Cu element is observable for the Cu foils obtained from the LIBs before cycling. According to Figure 5b–e, the existence of C and Sb elements in the Cu foil confirmed the migration of C and Sb atoms from the active materials layer to the Cu foil. Also, the content of C atoms is larger than that of Sb, suggesting the rapid migration rate of C atoms than Sb due to the small diameter of the atom. The migration distance into the original Cu foil increases with the cycle number, indicating that the discharge/charge process mainly drives this atom migration. In addition, the content of the Cu element is larger than that of the C and Sb elements in the Cu foil, and the content of the C and Sb element is larger than that of the Cu element in the new-formed porous film of Li_2SbCu, which is likely caused by the continuous corrosion of Cu foil in the electrolyte and the reaction among Li, Sb, and Cu atoms. The spatial distribution of C, Cu, and Sb in the porous film of Li_2SbCu after one cycle is similar to that after one hundred cycles, implying the repeated occurrence of the process mentioned above and reaction.

3.1.2. Mechanical Properties

The mechanical property of current collecting foil is very important for the reliability design and safety evaluation of the lithium-ion battery [37]. It is important to understand the mechanical behavior change of the current collector during cycling. The nano-indentation test is performed to investigate the local mechanical behavior of Cu foils after different cycles. Figure 6 shows the nominal contact modulus and hardness of Cu foils before and after different cycles. From Figure 6a, the contact modulus of the original copper foil is 48.75 GPa, which is consistent with the contact modulus of 50 GPa of the copper foil used as a fluid collector in the literature [38]. The nominal contact modulus of Cu foils after one cycle, ten, and thirty cycles is larger than that of the original Cu foil and increases with the cycle number, which is likely associated with the reinforcing effect of Li_2SbCu. When the full LIBs experience more than thirty cycles, the nominal contact modulus decreases with the cycle number caused by the continuous growth of porous structures. It is well known that surface roughness plays a crucial role in its indentation hardness, while the indentation hardness of a smooth surface is greater than that of a rough surface [39]. Figure 6b shows that the indentation hardness of the original copper collector is 0.95 GPa. The discharge/charge process increases the indentation hardness of Cu foils,

which is attributed to the strengthening effect of Li$_2$SbCu. Also, the indentation hardness of Cu foils increases with the cycle number when the full LIBs experienced less than thirty cycles and decreases with the cycle number when the cycle number is more than fifty, which is due to the excess growth of porous structures [39,40]. It is indicated that there exist two main factors, solution strengthening of Li$_2$SbCu and weakening effect of porous structure, affecting the mechanical performance of current collector during discharge/charge process.
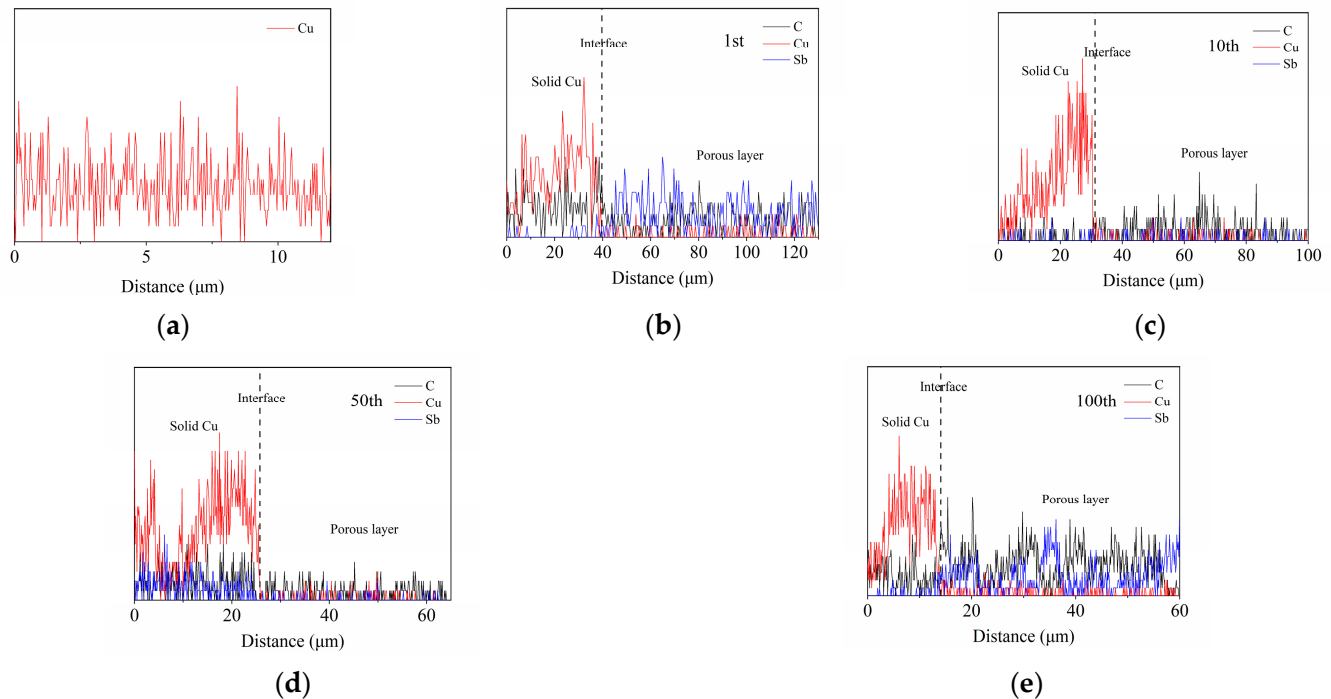
Figure 5. Element scan of Cu foils disassembled from the LIBs before (**a**) and after different cycles (**b**–**e**).
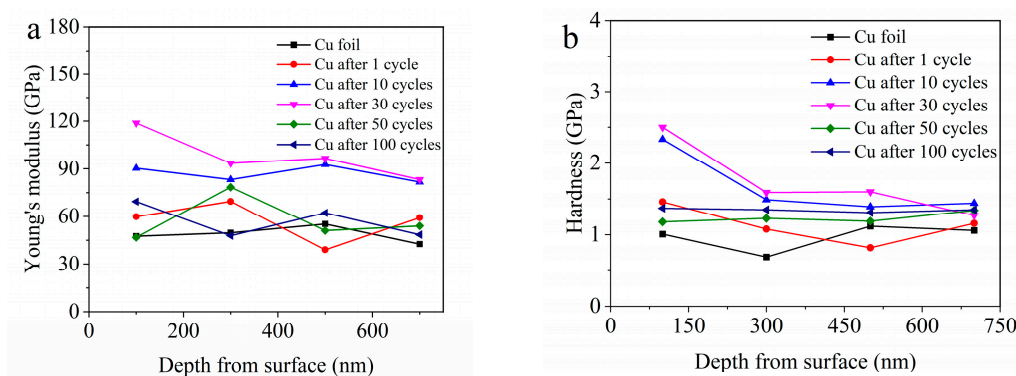
Figure 6. Nominal contact modulus (**a**) and indentation hardness (**b**) of Cu foils disassembled from the LIBs before and after different cycles.

3.2. Morphology, Structure, and Mechanical Performance Evolution of Al Current Collector during Cycling

3.2.1. Morphology and Structure Analysis

From Figure 7a, the diffraction peaks at 38.45°, 44.83°, 65.18°, and 78.03° correspond to the (1 1 1), (0 0 4), (2 0 8), and (1 1 1) crystal planes of Al, respectively. The peaks at 24.57° and 43.47° correspond to the (0 0 2) and (1 0 0) crystal planes of graphite carbon, respectively. Also, with the prolonging of the discharge/charge cycle, the peak shape of (0 0 2) peak of graphite carbon becomes narrow, and its intensity becomes strong. It indicates that the C atoms in the active materials layer migrate continuously into the Al

current collector during the discharge/charge process. The diffraction peaks at 19.58° and 31.93° correspond to the (1 1 1) and (2 2 0) crystal planes of Al_2O_3, respectively, and no peaks associated with Sb, Co, and Li can be found. The result suggests that there exists the migration of O atoms into Al current. These O atoms react with Al to produce the passivation layer of Al_2O_3 on the surface of Al foils.
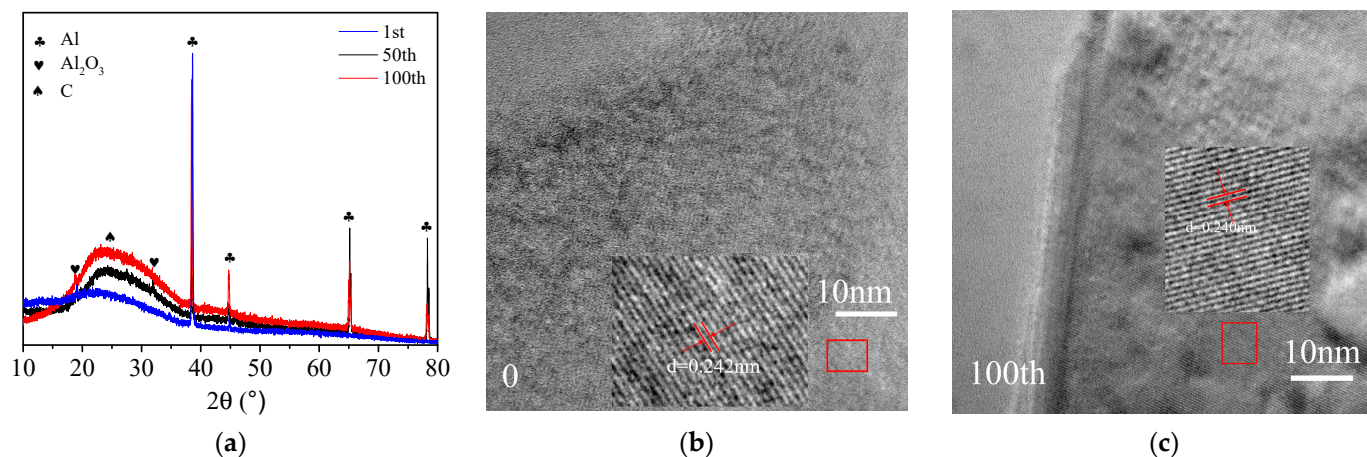

Figure 7. (**a**) XRD patterns of the Al current collector disassembled from LIBs after different discharge/charge cycles. HRTEM images of the Al foils disassembled from the LIBs before (**b**) and after (**c**) 100 cycles. The insert of (**b**,**c**) is enlarged portion of corresponding red area.

The HRTEM images of Al foils before and after 100 cycles are shown in Figure 7b,c. From Figure 7b, the lattice spacing is 0.242 nm, corresponding to a (3 1 1) crystal plane of Al_2O_3. After 100 cycles, the lattice fringe of 0.240 nm agrees well with the (3 1 1) crystal plane of Al_2O_3, in accordance with XRD results. This is associated with the formation of Al_2O_3 film on the surface of Al current collector.

Figure 8 shows the surface morphology of Al foils disassembled from the full LIBs before and after being discharged/charged to one cycle, ten, fifty, and one hundred cycles. Before the discharge/charge process, the Al foil shows a smooth and dense surface (Figure 8a), and no large morphology change is found after one cycle (Figure 8b). Increasing the cycle number to ten, some gullies appeared on the surface of Al foils (Figure 8c). When the LIBs are discharged/charged to fifty, there is an obvious decrease in the number of gullies on the surface of Al foils, while some small holes and cracks appear (Figure 8d). With increasing the cycle number to one hundred, more cracks are formed on the surface of Al foils and the size of cracks becomes large (Figure 8e). It is most likely that the discharge/charge potential promotes the decomposition of $LiPF_6$ salt, leading to the formation of more HF in the electrolyte solution and the rapid corrosion of Al foils, which finally caused the formation and growth of cracks [41,42]. Also, the corrosion of Al foils is related to the self-discharge of LIBs [43].
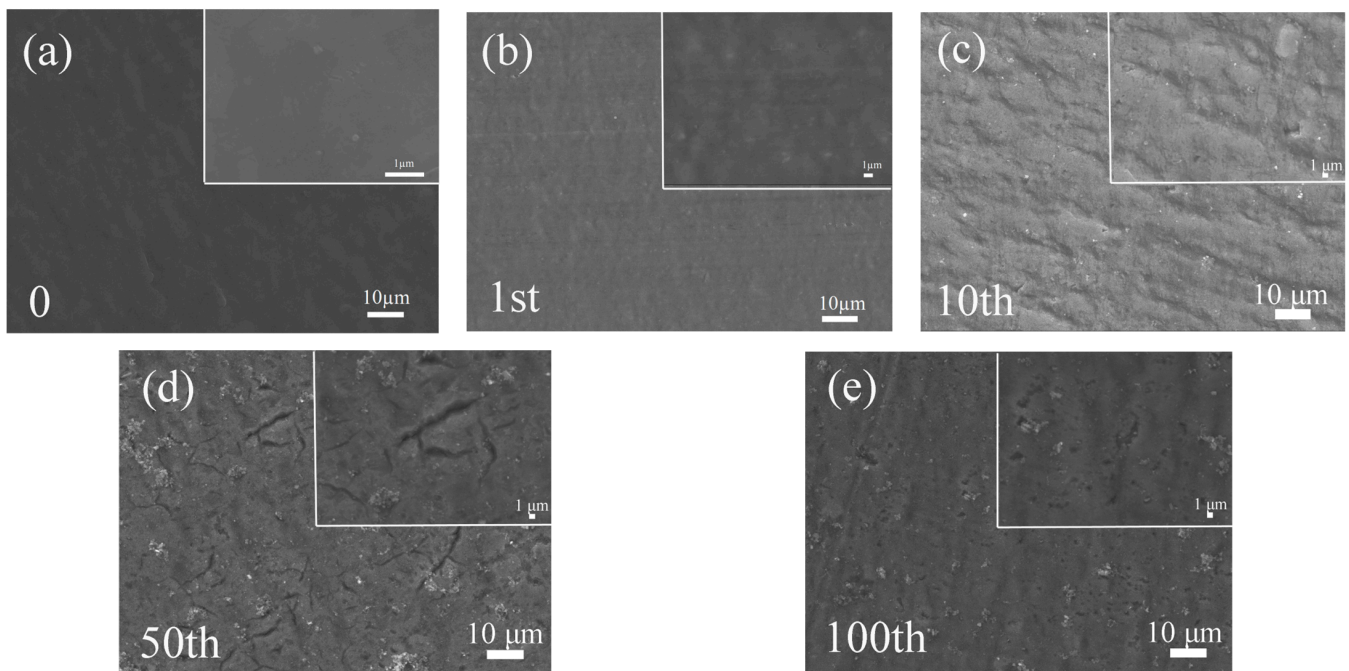
Figure 8. SEM microphotographs of the surface of Al foils disassembled from the LIBs before (**a**) and after (**b–e**) different cycles.

As observed in Figure 9, as expected, before the full LIBs are discharged/charged, the original Al foil has a smooth and dense cross microstructure (Figure 9a), which is similar to the Cu foil. After one cycle, a thin and relatively loose film of Al_2O_3 (Figure 9b) formed at the interface between the Al foil and the active materials layer. From Figure 9c,d, no significant separation or cracks can be found along with the interface between the Al foil and the Al_2O_3 film after ten and fifty cycles, which differ from the Cu foil in anode. It is indicated that the new-formed Al_2O_3 film is relatively stable, which is likely attributed to the stable structure of active materials in cathode. With the cycle number prolonged to one hundred, small gaps appeared at the interface between the Al foil and the Al_2O_3 film, and the Al_2O_3 film became relatively loose (Figure 9e). In addition, there exists the thickness change of the Al foil and the Al_2O_3 film during the discharge/charge process. As shown in Figure 9f, the thickness of the Al foil decreases and the thickness of the Al_2O_3 film increases with increasing the cycle number, which is attributed to the migration of Li, Co, and O to the Al foil and the dissolution of Al in the electrolyte.

Figure 10a,b show that there exist Co and O elements in the Al foil compared with the original Al foil before cycling. The amount of Co and O increases with increasing cycling. Also, the amount of Al is larger than that of Co and O atoms in the layer of Al foil, and the amount of Al is smaller than that of Co and O atoms in the film of Al_2O_3. All of these suggest the continuous dissolution of the Al foil and the migration of Li, Co, and O to the Al foil during the discharge/charge process. The morphology and structure change of Cu and Al foils will lead to the weak bond between the active material layer and the current collector, the decreased conductivity, and the thickness increase of current collector. All of these finally lead to the capacity and stability decrease of LIBs. The generation of the second phase will lead to the local mechanical behavior change of current collector.
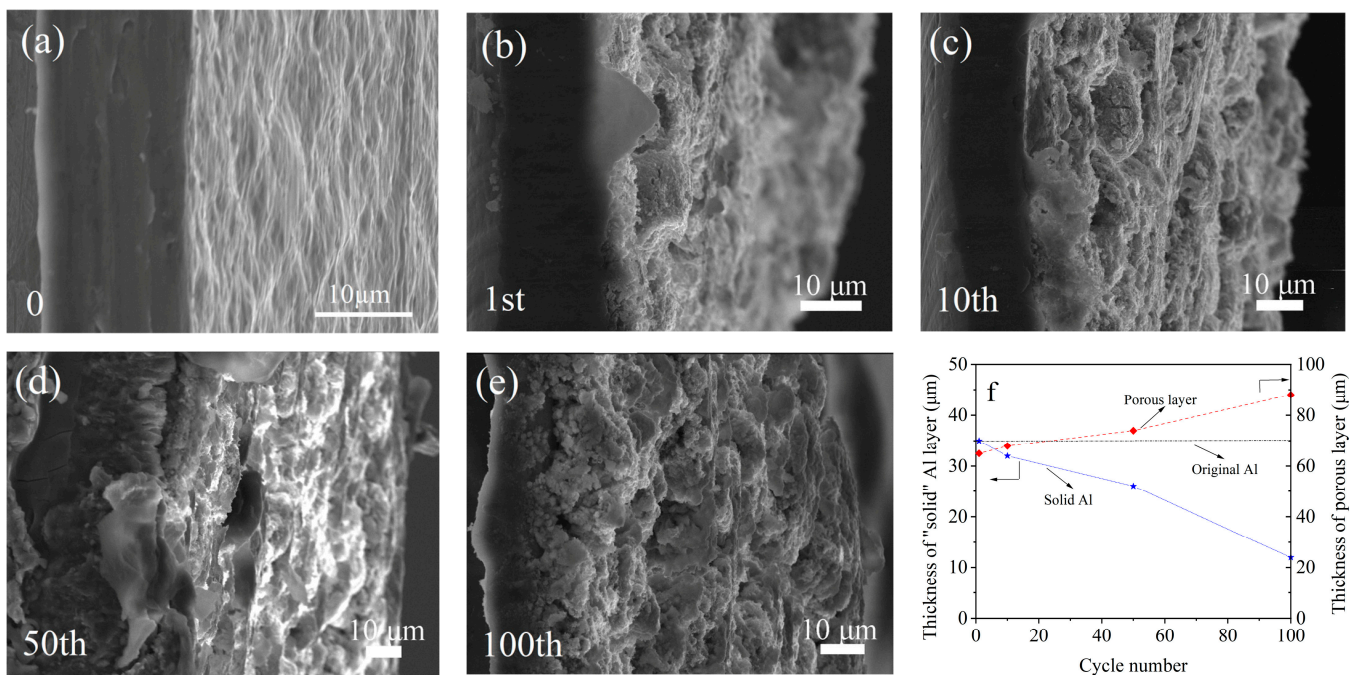
Figure 9. SEM microphotographs (**a**–**e**) of the cross-section of Al foils disassembled from the LIBs after different cycles, and (**f**) thickness change of the Al foil during discharge/charge process.
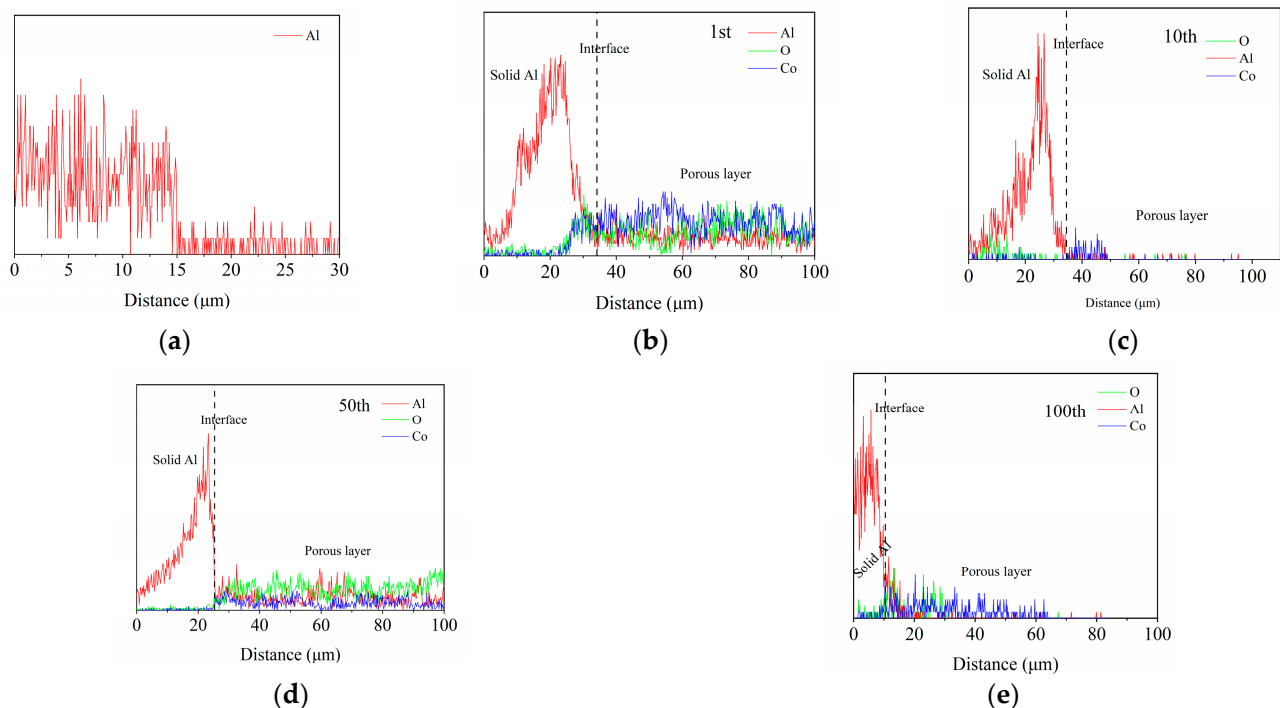

Figure 10. Element scan of Al foils disassembled from the LIBs before (**a**) and after different cycles (**b**–**e**).

3.2.2. Mechanical Properties

From Figure 11a,b, the local contact modulus is ~40 GPa for original Al foils and exhibits a tiny change for Al foils after one cycle, which should be related to the migration of carbon atoms and the formation of Al_2O_3. The discharge/charge process causes the continuous growth of the loose Al_2O_3 film, which leads to the gradual decrease of contact modulus and indention hardness of Al foils with the cycle number. When LIBs cycled more

than fifty cycles, no large change of the contact modulus and indentation hardness can be found. It may be attributed that the Al_2O_3 film on the surface of Al foil protects it from further rapid corrosion.
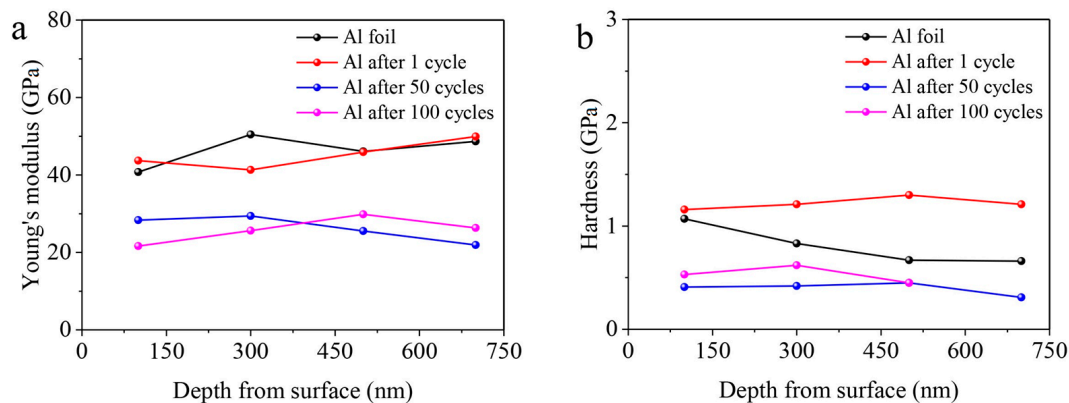
Figure 11. Nominal contact modulus (**a**) and hardness (**b**) of Al foils disassembled from the LIBs before and after different cycles.

At present, most of the research on the current collector mainly focuses on how to modify the current collector before cycling to improve its electrochemical performance [44–46]. The above conclusions describe the electrochemical-induced structure degradation of the current collector of lithium-ion batteries during cycling and found it plays an important key in cycling performance of Sb-based LIBs. This study provides an understanding of the capacity loss of Sb-based LIBs from the perspective of structural degradation of current collectors.

4. Conclusions

Here, we investigate the structure and mechanical changes of Cu and Al current collectors in Sb-based LIBs and analyze their contributions to the capacity decrease. The following conclusions can be summarized.

(1) There exists the migration of C, Sb, and Li atoms to the inside of Cu current collector, and the diffusion of Li, Co, and O atoms to the inside of Al current collector during cycling, which results in a porous film of Li_2SbCu and a relatively dense film of Al_2O_3 formed on the surface of Cu and Al current collector, respectively. The thickness of films increases with cycling.

(2) The formation of films leads to the poor conductivity and weak bond between active layer and current collector, and the increase of hardness of 0.84 GPa and modulus of 22.5 GPa for Cu current collector after 100 cycles, all of which finally results in the decrease of rate performance and cycling stability of LIBs.

(3) The restriction effect from cracks or poles of Al_2O_3 film leads to the smaller contact modulus and hardness of Al foils after cycles than the original Al foils. It caused hardness decrease of 0.53 GPa and modulus decrease of 18.93 GPa of Al current collector after 100 cycles, and no large change of the contact modulus and indentation hardness can be found after fifty cycles, which contributes to the improvement of cycling stability and charge capacity.

The study provides the understanding of the capacity loss of Sb-based LIBs from the perspective of structural degradation of current collectors during cycling. It indicates that this electrochemical-induced structure degradation plays an important key in battery performance, including the electric and mechanical connection between active materials layer and current collector, and the constriction to active materials layer. For a conventional electrode, the poor adhesion between the active layer and current collector may lead to mechanical and electrical failure. Therefore, the integrated current collector or freestanding

electrode can strengthen or avoid the cycling-induced interface instability, and is also a promising electrode structure for the improvement of cycling stability of LIBs.

Institutional Review Board Statement: Not applicable.

Informed Consent Statement: Not applicable.

Data Availability Statement: The authors confirm that the data supporting the findings of this study are available within the article.

Conflicts of Interest: The authors declare no conflict of interest.

References

1. Zinatloo-Ajabshir, S.; Morassaei, M.S.; Salavati-Niasari, M. Eco-friendly synthesis of Nd2Sn2O7-based nanostructure materials using grape juice as green fuel as photocatalyst for the degradation of erythrosine. *Compos. Part B Eng.* **2019**, *167*, 643–653. [CrossRef]
2. Shubha, J.P.; Adil, S.F.; Khan, M.; Hatshan, M.R.; Khan, A. Facile Fabrication of a ZnO/Eu2O3/NiO-Based Ternary Heterostructure Nanophotocatalyst and Its Application for the Degradation of Methylene Blue. *ACS Omega* **2021**, *6*, 3866–3874. [CrossRef] [PubMed]
3. Esfahani, M.H.; Zinatloo-Ajabshir, S.; Naji, H.; Marjerrison, C.A.; Greedan, J.E.; Behzad, M. Structural characterization, phase analysis and electrochemical hydrogen storage studies on new pyrochlore SmRETi2O7 (RE = Dy, Ho, and Yb) microstructures. *Ceram. Int.* **2022**, *49*, 253–263. [CrossRef]
4. Rezayeenik, M.; Mousavi-Kamazani, M.; Zinatloo-Ajabshir, S. CeVO4/rGO nanocomposite: Facile hydrothermal synthesis, characterization, and electrochemical hydrogen storage. *Appl. Phys. A* **2023**, *129*, 47. [CrossRef]
5. Scrosati, B.; Garche, J. Lithium batteries: Status, prospects and future. *J. Power Sources* **2010**, *195*, 2419–2430. [CrossRef]
6. Bai, Z.C.; Fan, N.; Sun, C.H.; Ju, Z.C.; Guo, C.L.; Yang, J.; Qian, Y.T. Facile synthesis of loaf-like ZnMn2O4 nanorods and their excellent performance in Li-ion batteries. *Nanoscale* **2013**, *5*, 2442–2447. [CrossRef]
7. Goriparti, S.; Miele, E.; De Angelis, F.; Di Fabrizio, E.; Zaccaria, R.P.; Capiglia, C. Review on recent progress of nanostructured anode materials for Li-ion batteries. *J. Power Sources* **2014**, *257*, 421–443. [CrossRef]
8. Parekh, M.H.; Parikh, V.P.; Kim, P.J.; Misra, S.; Qi, Z.M.; Wang, H.Y.; Pol, V.G. Encapsulation and networking of silicon nanoparticles using amorphous carbon and graphite for high performance Li-ion batteries. *Carbon* **2019**, *148*, 36–43. [CrossRef]
9. Wang, N.N.; Ma, X.J.; Xu, H.Y.; Chen, L.; Yue, J.; Niu, F.E.; Yang, J.; Qian, Y.T. Porous ZnMn2O4 microspheres as a promising anode material for advanced lithium-ion batteries. *Nano Energy* **2014**, *6*, 193–199. [CrossRef]
10. Roy, P.; Srivastava, S.K. Nanostructured anode materials for lithium ion batteries. *J. Mater. Chem. A* **2015**, *3*, 2454–2484. [CrossRef]
11. Guo, M.Q.; Zhang, X.G.; Bai, Z.C.; Ye, J.Y.; Meng, W.J.; Song, H.; Wang, Z.H. Hollow SnNi@PEO nanospheres as anode materials for lithium ion batteries. *Int. J. Hydrogen Energy* **2017**, *42*, 15290–15298. [CrossRef]
12. Meng, W.J.; Han, J.; Dang, Z.Z.; Li, D.; Jiang, L. Dual Doping of Titania for Enhanced Na Storage Performance. *ACS Appl. Mater. Interfaces* **2021**, *13*, 44214–44223. [CrossRef] [PubMed]
13. Meng, W.J.; Dang, Z.Z.; Li, D.S.; Jiang, L.; Fang, D.N. Efficient Sodium Storage in Selenium Electrodes Achieved by Selenium Doping and Copper Current Collector Induced Displacement Redox Mechanisms. *Adv. Funct. Mater.* **2022**, *32*, 2204364. [CrossRef]
14. Qian, J.F.; Chen, Y.; Wu, L.; Cao, Y.L.; Ai, X.P.; Yang, H.X. High capacity Na-storage and superior cyclability of nanocomposite Sb/C anode for Na-ion batteries. *Chem. Commun.* **2012**, *48*, 7070–7072. [CrossRef]

15. Ramireddy, T.; Rahman, M.M.; Xing, T.; Chen, Y.; Glushenkov, A.M. Stable anode performance of an Sb-carbon nanocomposite in lithium-ion batteries and the effect of ball milling mode in the course of its preparation. *J. Mater. Chem. A* **2014**, *2*, 4282–4291. [CrossRef]
16. Hou, H.S.; Zou, G.Q.; Ge, P.; Zhao, G.G.; Wei, W.F.; Ji, X.B.; Huang, L.P. Synergistic effect of cross-linked carbon nanosheet frameworks and Sb on the enhancement of sodium storage performances. *New J. Chem.* **2017**, *41*, 13724–13731. [CrossRef]
17. Han, Q.G.; Sheng, Y.L.; Han, Z.W.; Li, X.; Zhang, W.Q.; Li, Y.; Zhang, X. Metallic Sb nanoparticles embedded into a yolk-shell Sb2O3@TiO(2)composite as anode materials for lithium ion batteries. *New J. Chem.* **2020**, *44*, 13430–13438. [CrossRef]
18. Pan, Q.C.; Wu, Y.A.; Zhong, W.T.; Zheng, F.H.; Li, Y.P.; Liu, Y.Z.; Hu, J.H.; Yang, C.H. Carbon Nanosheets Encapsulated NiSb Nanoparticles as Advanced Anode Materials for Lithium-Ion Batteries. *Energy Environ. Mater.* **2020**, *3*, 186–191. [CrossRef]
19. Wang, C.; Chen, G.Y.; Kou, J.R.; Zhang, X.J.; Xu, X.X.; Bao, J.C.; Shen, Z.H.; Jin, X.; Zhang, H.G.; Liu, L.; et al. Sb@S-N-C nanocomposite as long-cycle stable anode material for lithium ion batteries. *J. Alloys Compd.* **2020**, *814*, 152161. [CrossRef]
20. Li, H.; Shi, L.H.; Wang, Q.; Chen, L.Q.; Huang, X.J. Nano-alloy anode for lithium ion batteries. *Solid State Ion.* **2002**, *148*, 247–258. [CrossRef]
21. Park, M.G.; Lee, D.H.; Jung, H.; Choi, J.H.; Park, C.M. Sn-Based Nanocomposite for Li-Ion Battery Anode with High Energy Density, Rate Capability, and Reversibility. *ACS Nano* **2018**, *12*, 2955–2967. [CrossRef] [PubMed]
22. Cohen, Y.S.; Yair Cohen, A.; Aurbach, D. Micromorphological Studies of Lithium Electrodes in Alkyl Carbonate Solutions Using in Situ Atomic Force Microscopy. *J. Phys. Chem. B* **2000**, *104*, 12282–12291. [CrossRef]
23. Lucas, I.T.; Pollak, E.; Kostecki, R. In situ AFM studies of SEI formation at a Sn electrode. *Electrochem. Commun.* **2009**, *11*, 2157–2160. [CrossRef]
24. Walter, M.; Doswald, S.; Krumeich, F.; He, M.; Widmer, R.; Stadie, N.P.; Kovalenko, M.V. Oxidized Co-Sn nanoparticles as long-lasting anode materials for lithium-ion batteries. *Nanoscale* **2018**, *10*, 3777–3783. [CrossRef] [PubMed]
25. Lamiel, C.; Hussain, I.; Ma, X.; Zhang, K. Properties, functions, and challenges: Current collectors. *Mater. Today Chem.* **2022**, *26*, 101152. [CrossRef]
26. Kim, Y.-L.; Sun, Y.-K.; Lee, S.-M. Enhanced electrochemical performance of silicon-based anode material by using current collector with modified surface morphology. *Electrochimica Acta* **2008**, *53*, 4500–4504. [CrossRef]
27. Wu, Y.; Huang, P.; Gao, L.T.; Guo, Z.-S. Modeling Contact Behavior of Multiparticles and Particle–Current Collector Contact in Porous Electrode. *Energy Technol.* **2022**, *10*, 2200786. [CrossRef]
28. Zhang, J.; Zuo, D.; Pei, X.; Mu, C.; Chen, K.; Chen, Q.; Hou, G.; Tang, Y. Effects of Electrolytic Copper Foil Roughness on Lithium-Ion Battery Performance. *Metals* **2022**, *12*, 2110. [CrossRef]
29. Shin, D.-Y.; Park, D.-H.; Ahn, H.-J. Interface modification of an Al current collector for ultrafast lithium-ion batteries. *Appl. Surf. Sci.* **2019**, *475*, 519–523. [CrossRef]
30. Sung, K.; Kim, K.; Ahn, H. Carbon quantum dot-laminated stepped porous Al current collector for stable and ultrafast lithium-ion batteries. *Int. J. Energy Res.* **2022**, *46*, 8989–8999. [CrossRef]
31. Reyter, D.; Rousselot, S.; Mazouzi, D.; Gauthier, M.; Moreau, P.; Lestriez, B.; Guyomard, D.; Roue, L. An electro-chemically roughened Cu current collector for Si-based electrode in Li-ion batteries. *J. Power Sources* **2013**, *239*, 308–314. [CrossRef]
32. Wu, M.; Kim, J.Y.; Chae, O.B.; Jung, W.B.; Choi, S.; Kim, D.Y.; Suk, J.; Gereige, I.; Kang, Y.; Jung, H.T. Na-noscale Wrinkled Cu as a Current Collector for High-Loading Graphite Anode in Solid-State Lithium Batteries. *ACS Appl. Mater. Interfaces* **2021**, *13*, 2576–2583. [CrossRef]
33. Guo, M.; Meng, W.; Zhang, X.; Bai, Z.; Wang, G.; Wang, Z.; Yang, F. Structural Degradation of Cu Current Collector During Electrochemical Cycling of Sn-Based Lithium-Ion Batteries. *J. Electron. Mater.* **2019**, *48*, 7543–7550. [CrossRef]
34. Hyams, T.C.; Go, J.; Devine, T.M. Corrosion of Aluminum Current Collectors in High-Power Lithium-Ion Batteries for Use in Hybrid Electric Vehicles. *J. Electrochem. Soc.* **2007**, *154*, C390–C396. [CrossRef]
35. Guo, M.; Chen, J.; Meng, W.; Cheng, L.; Bai, Z.; Wang, Z.; Yang, F. Sb nanocrystal-anchored hollow carbon microspheres for high-capacity and high-cycling performance lithium-ion batteries. *Nanotechnology* **2019**, *31*, 135404. [CrossRef]
36. Jin, K.; Kobayashi, K. Anodic polarization behavior of copper in propylene carbonate. *J. Power Sources* **2001**, *101*, 47–52. [CrossRef]
37. Cheng, F.-L.; Yang, W.-K.; Luo, X.-M.; Zhang, G.-P. Geometrical size effect on tensile properties of ultrathin current collector foils for lithium-ion batteries. *J. Mater. Res.* **2022**, *37*, 3708–3719. [CrossRef]
38. Zhu, J.; Feng, J.; Guo, Z. Mechanical properties of commercial copper current-collector foils. *RSC Adv.* **2014**, *4*, 57671–57678. [CrossRef]
39. Chen, L.; Ahadi, A.; Zhou, J.M.; Stahl, J.E. Modeling effect of surface roughness on nanoindentation tests. In Proceedings of the 14th CIRP Conference on Modeling of Machining Operations (CIRP CMMO), Torino, Italy, 13–14 June 2013; pp. 334–339.
40. Shi, X.; Polycarpou, A.A. Measurement and Modeling of Normal Contact Stiffness and Contact Damping at the Meso Scale. *J. Vib. Acoust.* **2005**, *127*, 52–60. [CrossRef]
41. Peng, C.; Yang, L.; Zhang, Z.; Tachibana, K.; Yang, Y.; Zhao, S. Investigation of the anodic behavior of Al current collector in room temperature ionic liquid electrolytes. *Electrochimica Acta* **2008**, *53*, 4764–4772. [CrossRef]
42. Kramer, E.; Passerini, S.; Winter, M. Dependency of Aluminum Collector Corrosion in Lithium Ion Batteries on the Elec-trolyte Solvent. *ECS Electrochem. Lett.* **2012**, *1*, C9–C11. [CrossRef]

43. Ma, D.; Song, Z.H.; Zhang, H.Z.; Hussain, A.; Feng, K.; Zhang, H.M.; Li, X.F. An all-weather Li/LiV2(PO4)(3)primary battery with improved shelf-life based on thein situmodification of the cathode/electrolyte interface. *J. Mater. Chem. A* **2020**, *8*, 16951–16959. [CrossRef]

44. Chen, L.; Chen, G.; Lin, X.; Zheng, Z.; Wen, Z.; Wu, D.; Weng, Z.; Zhang, N.; Liu, X.; Ma, R. Lithiophilic and Anticorrosive Cu Current Collector via Dual-Bonded Porous Polymer Coating for Stable Lithium-Metal Batteries. *ACS Appl. Mater. Interfaces* **2023**, *15*, 10273–10282. [CrossRef] [PubMed]

45. Wang, J.; An, Y.; Shen, H.; Man, Q.; Feng, J. Flexible and ultralight MXene paper as a current collector for microsized porous silicon anode in high-energy lithium-ion batteries. *2D Mater.* **2023**, *10*, 014010. [CrossRef]

46. Chun, J.; Wang, X.; Zhang, Y.; Wei, C.; Wang, Z.; Feng, J. Ti3C2Tx film current collectors for high-performance sodium-ion batteries. *Vacuum* **2023**, *207*, 111476. [CrossRef]